Research Article | Vol. 27, No. 18 | 2 Sep 2019 | OPTICS EXPRESS 25228
Optics EXPRESS

Direct observation of OAM correlations from spatially entangled bi-photon states

ZEFERINO IBARRA-BORJA,[1] CARLOS SEVILLA-GUTIÉRREZ,[1,2] ROBERTO RAMÍREZ-ALARCÓN,[1,*] QIWEN ZHAN,[2,3] HECTOR CRUZ-RAMÍREZ,[4] AND ALFRED B. U'REN[4]

[1] *Centro de Investigaciones en Óptica A.C., Loma del Bosque 115, Colonia Lomas del Campestre, 37150 León Guanajuato, México*
[2] *Department of Electro-Optics and Photonics, University of Dayton, Dayton, Ohio 45469, USA*
[3] *School of Optical-Electrical and Computer Engineering, University of Shanghai for Science and Technology, Shanghai 200093, China*
[4] *Instituto de Ciencias Nucleares, Universidad Nacional Autónoma de México, Apartado Postal 70-543, 04510 DF, México*
[*] *roberto.ramirez@cio.mx*

Abstract: We present spatially-resolved observations of orbital angular momentum (OAM) conservation, via a Laguerre-Gauss (LG) basis decomposition, of spatially-entangled photon pairs produced in type-I collinear spontaneous parametric downconversion (SPDC). These results were obtained with a novel detection system for OAM-entangled photon pairs that combines a projective measurement for the signal photon to a specific value of the azimuthal index l_s, with a spatially-resolved measurement for the idler photon using an intensified charge coupled (ICCD) camera. In combination with far-field diffraction of the idler photon through a triangular aperture, we are able to obtain: i) the spatial structure of the heralded idler photon, as governed by the user-selected topological charge of the signal photon; ii) the OAM spectrum; and iii) the topological charge (both magnitude and sign) for the heralded idler photon.

1. Introduction

The study of light carrying orbital angular momentum (OAM) has attracted much attention over the last 25 years on account of its very broad field of applications in novel technologies, such as optical trapping [1–3], optical manipulation [4], and communications [5]. Particularly for optical communications, the use of OAM is tremendously advantageous since it permits straightforward scaling to higher dimensions, in contrast to polarization which is limited to a dimension of 2.

In the quantum domain, the application of OAM started with the confirmation that a photon can carry a well-defined value of OAM [6], followed by the theoretical [7, 8] and experimental [9] demonstrations that the process of spontaneous parametric down conversion (SPDC) under conditions of azimuthal symmetry preserves OAM, which can result in the generation of photon pairs entangled in the OAM degree of freedom. Following these works, there have been significant efforts oriented at understanding and using the OAM degree of freedom in a variety of novel applications in quantum optics such as the demonstration of the violation of Bell inequalities [10–12], ghost imaging [13], and the imaging of entanglement using polarization [14].

Laguerre-Gauss (LG) modes, with an azimuthal mode index l and an electric field amplitude proportional to $\exp(il\phi)$, carry orbital angular momentum $\hbar l$. Most studies of OAM in SPDC photon pairs have employed the Laguerre-Gauss (LG) basis due to the ease with which the quantum state can be projected onto particular LG modes [9, 15–19]. The SPDC bi-photon state has also been studied in the context of other families of modes such as Bessel-Gauss modes [20–24]. The usual experimental techniques applied to prove the presence of OAM correlations and entanglement are based on the projection of each photon in a given pair onto

#356392 https://doi.org/10.1364/OE.27.025228
Journal © 2019 Received 3 Jan 2019; revised 23 May 2019; accepted 24 May 2019; published 22 Aug 2019

Optics EXPRESS

an LG mode with a particular azimuthal index l: an appropriate phase mask first converts the desired mode to a Gaussian mode, to be discriminated from other modes by collection into a single-mode optical fiber. This approach, initially implemented with holographic gratings [9] and later with more versatile phase holograms displayed on spatial light modulators (SLM) [15], serves as an OAM mode discriminator which, however, is incapable of fully probing the complete spatial distribution of the entangled LG modes.

In this work we exploit recent advances in two-dimensional detector arrays with sensitivity at the single-photon level so as to improve the detection capabilities of photon pairs carrying OAM. By integrating a commercially-available intensified charged coupled (ICCD) camera into a typical SLM-based experimental configuration [15, 16], we are able to spatially-resolve the idler photon, heralded by the detection of a signal photon with a particular value of the azimuthal index l_s, and thus projected to an LG mode with a specific OAM value $l_i = -l_s$. Our setup thus allows us to *directly visualize* OAM correlations, consistent with OAM conservation, in addition to obtaining the OAM spectrum, i.e. the values of the expansion coefficients of the bi-photon state when expressed in the LG basis, that other experiments have already reported. So as to unequivocally determine the topological charge (magnitude as well as sign) of the heralded idler photon, in addition we have performed an experiment based on single-photon diffraction through a triangular aperture. Our work allows for a richer appreciation of the full transverse structure of spatially-entangled bi-photon states and can be exploited in quantum communications and quantum imaging implementations, for which spatially-resolved measurements at the single photon level are required.

2. Theory

It is well known that under certain conditions, see below, the process of spontaneous parametric down conversion (SPDC) conserves orbital angular momentum (OAM) at the single photon level [9]. The OAM conservation rule involving the pump (p), signal (s), and idler (i) modes can be written as [8, 17]

$$\hbar l_p = \hbar l_s + \hbar l_i, \tag{1}$$

where $\hbar l_j$, with $j = p, s, i$ and with l_j the azimuthal index of the mode, represents the OAM carried by the photons involved in the SPDC process. As is the case for transferring the angular spectrum from the pump beam to a heralded single photon [22, 25], OAM conservation, i.e Eq. (1), occurs only under certain specific conditions. It has been found that OAM conservation is fulfilled if: i) all the wavevectors emitted in the SPDC process are collected, or ii) if only a portion of the emission cone is collected in a noncollinear configuration, then specific constraints must be fulfilled by the values of the crystal length, the pump beam waist, and the aperture angle of the SPDC cone [21, 26]. In view of this, the easiest way to preserve OAM is to employ a setup utilising SPDC emission in a collinear fashion from a type-I downconversion source while collecting all the emitted wavevectors, which is precisely the configuration exploited in this work.

The two-photon state in the OAM degree of freedom, decomposed into Laguerre-Gauss modes, can be written as [18]

$$|\Psi\rangle_{SPDC} = \sum_{l_s,p_s} \sum_{l_i,p_i} C_{l_s,l_i}^{p_s,p_i} |l_s, p_s\rangle |l_i, p_i\rangle, \tag{2}$$

where $|l_j, p_j\rangle_j$ represents a single photon in an LG mode with azimuthal index l and radial index p, for the signal (s) or idler (i) photon, with $j = s, i$. The coefficients $\left|C_{l_s,l_i}^{p_s,p_i}\right|^2$ then represent the probability of creating a photon pair with a signal mode $|l_s, p_s\rangle_s$ and an idler mode $|l_i, p_i\rangle_i$. The LG modes $LG_{l,p}(\rho, \phi, z) = \langle \overline{r}|l, p\rangle$ represent the OAM basis states which, in cylindrical coordinates, at the beamwaist (z=0) can be written as [27]

Optics EXPRESS

$$LG_{l,p}(\rho,\phi) = \sqrt{\frac{2p!}{\pi(p+|l|)!}}\frac{1}{w_0}\left(\frac{\rho\sqrt{2}}{w_0}\right)^{|l|}\exp\left(\frac{-\rho^2}{w_0^2}\right)L_p^{|l|}\left(\frac{2\rho^2}{w_0^2}\right)\exp(il\phi), \tag{3}$$

where w_0 represents the Gaussian beam waist and the associated Laguerre polynomials $L_p^{|l|}$ are

$$L_p^{|l|}(x) = \sum_{i=0}^{p}(-1)^i\frac{(p+|l|)!}{(p-i)!(|l|+i)!i!}x^i. \tag{4}$$

This decomposition is particularly convenient because the LG modes are eigenstates of the orbital angular momentum operator $\hat{L}_z$, producing photon states with a definite OAM value $\hbar l$ [28]. Now, the various LG modes with a specific l-index but with different p indices are degenerate in their OAM value and cannot be discriminated in our experiment (described below). We refer to the resulting superpositions of p values with a fixed l value as spiral harmonics, expressed as

$$C_{l_j}|l_j\rangle_j = \sum_{p_j} C_{l_j}^{p_j}|l_j,p_j\rangle_j. \tag{5}$$

In terms of the spiral harmonics, we can re-writte Eq. (2) as

$$|\Psi\rangle_{SPDC} = \sum_{l_s}\sum_{l_i} C_{l_s,l_i}|l_s\rangle_s|l_i\rangle_i. \tag{6}$$

OAM conservation implies that the bi-photon state is entangled in the OAM degree of freedom. In order to see this, consider the case of a Gaussian pump beam ($l_p = 0$), so that $l_s = -l_i = l$. In this case, Eq. (6) becomes

$$|\Psi\rangle_{SPDC} = \sum_{l=0}^{\infty}\left(C_{l,-l}|l\rangle_s|-l\rangle_i + C_{-l,l}|-l\rangle_s|l\rangle_i\right). \tag{7}$$

In this work we carry out spatially-resolved measurements of the idler photon, as heralded by the detection of the signal photon in a specific l_s Laguerre-Gauss mode.

3. Experiment

The experimental setup is shown in Fig. 1. As SPDC photon pair source we have used a 2mm-thick β-barium borate (BBO) crystal cut for type-I downconversion. The crystal is pumped by a CW diode laser (PB) centered at a wavelength of 405.2 nm (Crystalaser DL-405-100), to produce collinear, frequency degenerate photon pairs. The spatial transverse mode of the diode laser is filtered by coupling into a single mode fiber (SMF) in order to produce a Gaussian mode with a power of $50mW$. Prior to reaching the nonlinear crystal, the polarization of the pump beam incident upon the crystal is controlled with a half wave plate (HWP) and then focused with lens L_1 (with focal length $f_1 = 1000mm$), resulting in a beam waist radius of $w_0 = 310\mu m$ on the crystal plane.

In order to spectrally filter the generated photon pairs we use the BPF element composed of a long-pass filter which transmits wavelengths $\lambda > 500nm$ (Thorlabs FELH0500), followed by a band pass filter centered at $810nm$ with $10nm$ bandwidth (Thorlabs FBH810-10). The collinear SPDC emission at the crystal plane is imaged onto two equivalent image planes (IP_1, IP_3) using a bifurcated 4f telescope with 3.33x magnification, formed by plano-convex lens L_2 ($f_2 = 75mm$), plano-convex lenses L_3 ($f_3 = 250mm$) and a 50 : 50 beam splitter BS (Thorlabs BS017). One of the crystal image planes (IP_1) forms on the focal plane of an image-preserving optical delay line (OD), which propagates the image plane to the detection plane (FP_1) of an ICCD camera (Andor

Optics EXPRESS

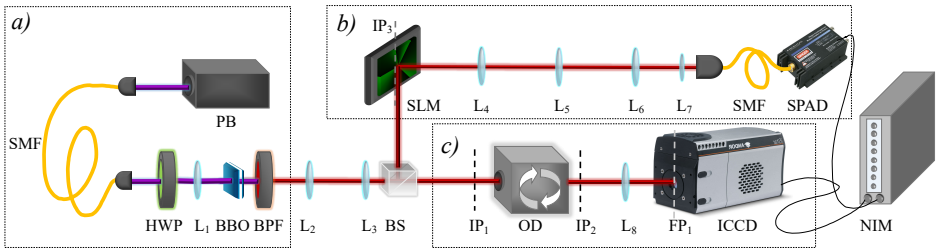

Fig. 1. Experimental setup consisting of: a) Collinear type-I SPDC photon pair source. b) OAM single photon spatial mode projector, and c) Spatially-resolved heralded idler photon detection system. After being separated by a 50:50 beam splitter (BS), the signal photon interacts with the phase mask displayed on the SLM, placed in the image plane (IP_3) of the crystal and is detected by a bucket detector in the form of a SPAD. The idler photon is detected in the far-field (FP_1) by a spatially-resolved array detector in the form of an ICCD camera.

iStar 334T), placed in the far-field of the crystal [29]. Another crystal image plane (IP_3) is set to coincide with a spatial light modulator SLM (Holoeye HES-6010-NIR), which is part of an OAM single photon spatial mode projector. The photons propagating through the bucket detector and spatially-resolved detector arms are labelled as signal and idler photons respectively.

In this work, we want to experimentally determine the decomposition coefficients of the two-photon state in the Laguerre-Gauss basis, while directly visualizing the OAM correlations between the signal and idler photons. In particular, we carry out direct two-dimensional measurements of the idler photon's spatial mode, as heralded by the detection of its correlated signal photon in a Laguerre-Gauss mode with a specific l_s-index (Eq. (7)). The photon propagating through the OAM single photon spatial mode projector travels in a superposition of spiral harmonics with a range of l_s values. On the SLM, each spiral harmonic (defined by a particular value of l_s) is selectively converted into a $l_s = 0$ Gaussian mode by displaying a spiral phase hologram with $l = -l_s$ dislocations, such as the ones shown in Fig. 2, so as to remove the phase singularity [15, 30].

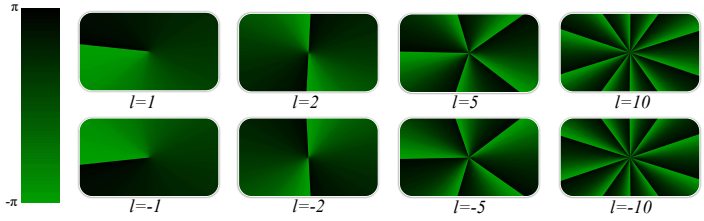

Fig. 2. Phase masks displayed on the SLM used to convert the $l_s = -l$ signal photon Laguerre-Gauss component into a $l_s = 0$ Gaussian mode.

The image plane coinciding with the SLM is then re-imaged onto the input of a single mode fiber (SMF) using a system of two consecutive demagnifying 4f telescopes, coupling only the desired l_s component of the signal photon, appropriately converted into a Gaussian mode by the SLM. This Gaussian mode obtained for the desired l_s value is then collected by the SMF, and subsequently detected by a single photon avalanche photodiode SPAD (Excelitas SPCM-AQRH), with its TTL output pulse discriminated and electronically delayed using NIM modules (Phillips Scientific PS-704 and PS-792) and used for triggering the spatially-resolved heralded idler

photon detection system, composed of the OD and the ICCD camera. The lenses composing the demagnifying 4f telescopes were chosen so as to maximize the number of counts detected by the SPAD and the number of modes observed by the ICCD camera in the far-field (FP_1). By using plano convex lenses L_4 ($f_4 = 300mm$), L_5 ($f_5 = 60mm$), L_6 ($f_6 = 1000mm$) and aspheric lens L_7 ($f_7 = 8mm$), up to 4300 singles counts per second were registered by the SPAD and high-quality images were obtained for l_s up to $l_s = \pm 10$.

In order to test the operation of the OAM single photon spatial mode projector we implemented a backward-propagating version of our detection system, as in the Klyshko's advanced-wave picture (AWP), by replacing the heralding detector with a classical source, in this case by coupling a $808nm$ diode laser into the SMF [31, 32]. Figure 3 shows the far-field transverse spatial mode distribution produced by the SLM when illuminated by a Gaussian beam, as detected in the far-field of the crystal on the ICCD camera, which by the AWP constitutes an effective simulation of the behaviour of the entangled photon pairs.

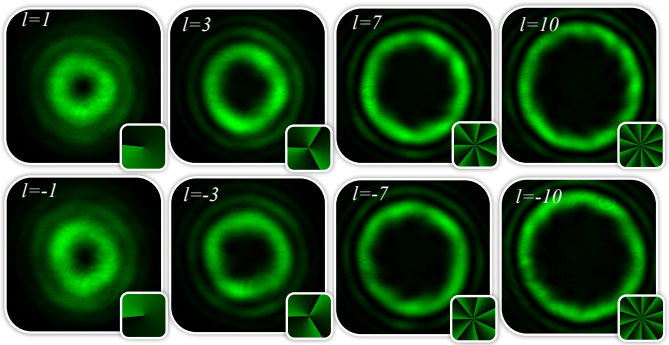

Fig. 3. Laguerre-Gauss spatial modes carrying a definite OAM value with the corresponding l-index. The modes were generated by the SLM with the phase masks shown in Fig. 2 (shown also here as insets). This backward-propagating scenario demonstrates the correct operation of the OAM spatial mode projector.

Once we select a Laguerre-Gauss component with a specific OAM value (l_s-index) for the signal photon, we spatially-resolve the heralded photon by opening a detection window at the precise time of arrival of the idler photon at the ICCD camera plane (FP_1 in Fig. 1). To do so, in our experiment we had to overcome a considerable delay to trigger the ICCD by implementing an image-preserving optical delay line (OD in Fig. 1) of around $28m$ and a total propagation time of around $90ns$, as explained in Appendix A [29].

We have performed the described measurement using the SPDC photon pairs, selecting values up to $l_s = \pm 10$ for the signal photon LG mode, by displaying the corresponding phase mask on the SLM, and observing with the ICCD camera the spatial structure for the heralded idler photon. Figure 4 presents selected cases of the images obtained; for the complete set of measurements the reader is referred to Fig. 10 ($l_s \leq 0$) and Fig. 11 ($l_s \geq 0$) in Appendix B. From Fig. 4 it is clear that the user-selected value of l_s is correlated with the spatial structure observed for the idler photon, suggesting the relationship $l_i = -l_s$, but as may be seen from the two columns in Fig. 4, the sign of the resulting l_s cannot be inferred from these measurements.

Since the ICCD camera records the coincidence count rate per pixel, we not only obtain the transverse intensity profile, but also the total coincidence detection rate by summing over all the pixels. This constitutes a measurement of the coefficients $\left|C_{(l,-l)}\right|^2$ of the Laguerre-Gauss basis expansion Eq. (7) of our photon pair state. In Fig. 5 the total number of coincidences per minute are shown as a function of the selected l_s LG mode for the signal photon, where it is evident that

Optics EXPRESS

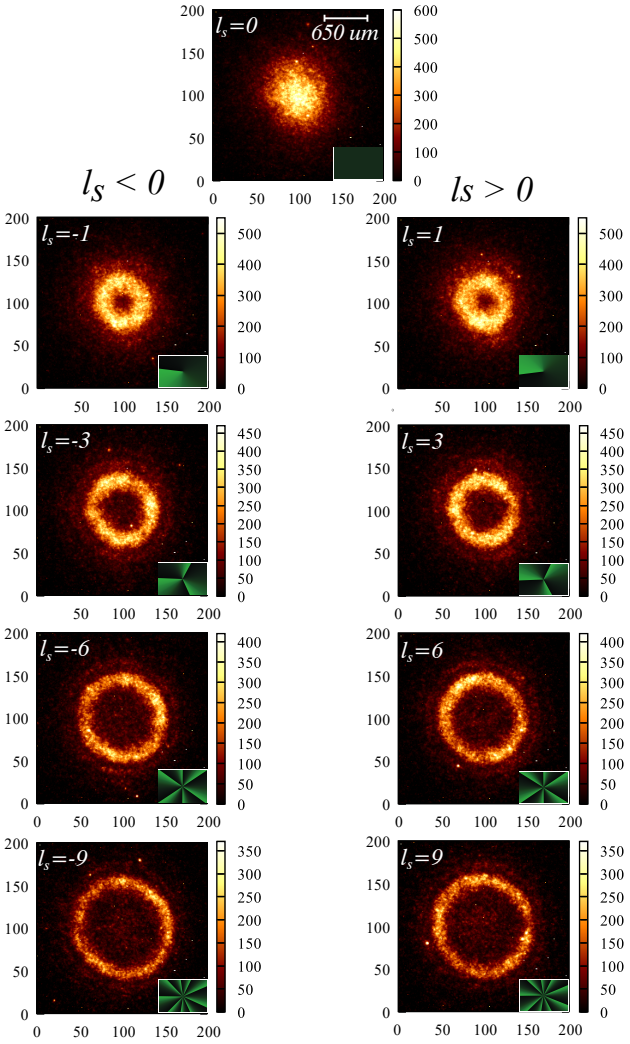

Fig. 4. Coincidence count rate recorded by the ICCD, representing the far-field transverse intensity distribution of the heralded idler photon for l_s values selected with the OAM spatial mode projector. The axes of the plots represent the camera pixels, with the corresponding scale shown for the $l_s = 0$ case, and the colorbars are expressed in coincidences per minute. The inset shows the phase mask displayed on the SLM.

the probability amplitude decreases with the azimuthal index l. From these measurements, it is clear that the detection rates with topological charge l and $-l$ are approximately equal, meaning that $\left|C_{(l,-l)}\right|^2 \approx \left|C_{(-l,l)}\right|^2$, which can be observed in the decaying symmetry of the probability amplitude about $l_i = 0$. Note that it is known that using a pump beam with topological charge $\pm l_p$ the behavior would be the same but shifted by $\pm l_p$ units [9].

While the results in Fig. 4 show the characteristic vortex structure of the heralded idler photon in a Laguerre-Gauss spatial mode, they do not yield the topological charge. In order to obtain such information, we exploit an OAM measurement technique to determine the topological

Optics EXPRESS

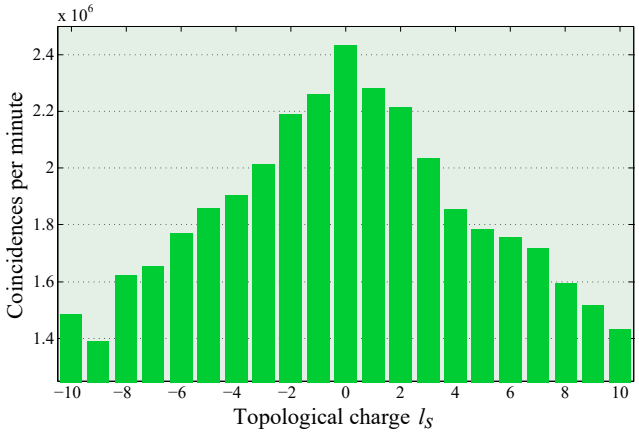

Fig. 5. Measured coefficients $\left|C_{(l,-l)}\right|^2$ of the bi-photon state Laguerre-Gauss basis expansion in Eq. (7), for azimuthal coefficients $l_i = -l_s$.

charge of an optical vortex beam through far-field diffraction by an equilateral triangular aperture (TA) [23, 24, 33, 34]. When the phase singularity of a vortex beam is aligned with the center of a vertically-oriented TA (with one side of the triangle parallel to the optical table), the far field diffraction pattern produces a triangular arrangement of intensity lobes rotated ±30° from the vertical axis. The magnitude of the topological charge l is given by $N - 1$, where N is the number of lobes on any side of the triangular intensity pattern and the sign is determined by the direction of the rotation. Patterns rotated anticlockwise correspond to positive topological charges ($l > 0$) whereas patterns rotated clockwise correspond to negative topological charges ($l < 0$) [33]. In this manner we can ascertain the presence of OAM and determine the topological charge of the diffracted photon, in our case the heralded idler photon.

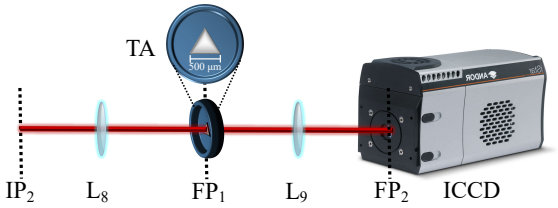

Fig. 6. Setup for measuring the topological charge of the heralded idler photon, with a front view of the TA showing the lateral dimensions and orientation.

In order to implement the topological charge measurement we use the setup shown in Fig. 6, placing a TA with sides of $500\mu m$ length on the camera plane (FP_1), corresponding to the Fourier transform of the propagated crystal plane (IP_2), created after L_8. So as to observe the diffracted far-field transverse intensity pattern, we place lens L_9 (focal length $f_9 = 100mm$) a distance of $100mm$ from the TA plane, defining a new camera plane (FP_2), a distance of $100mm$ from the lens, where we now place the ICCD camera. In order to adjust the size of the signal-photon intensity pattern to the dimensions of the TA, with $500\mu m$ side, we used a lens L_8 with an appropriate focal length for each value of l_s (and l_i as given by $l_i = -l_s$). For the measurements shown in Fig. 7, corresponding to $l_s = \pm 1$, we used a lens L_8 with focal length $f_8 = 250mm$. For the measurement corresponding to $l_s = \pm 2$, we used a L_8 with focal length $f_8 = 150mm$. Note that in this measurement the transverse positioning of the TA is critical and must be centered on

Optics EXPRESS

the mode singularity; the reader is referred to Appendix C for details on how this is performed. The resulting diffraction intensity patterns recorded by the ICCD, triggered by the detection of the signal photon, are shown in Fig. 7. These measurements reveal the topological charge of the heralded idler photon.

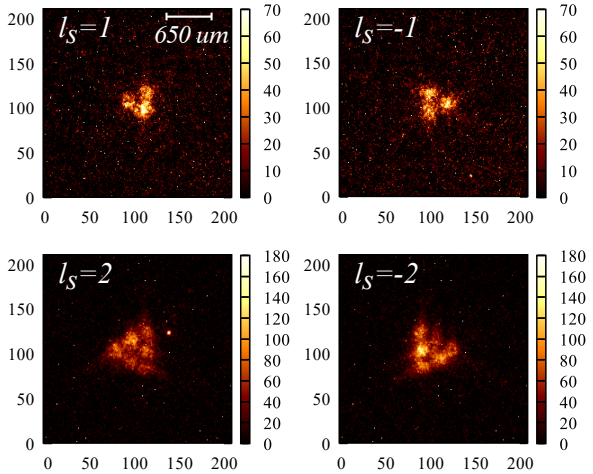

Fig. 7. Coincidence count rate recorded by the ICCD, representing the far-field diffraction pattern of the heralded idler photon from the TA, for the cases of $l_s = \pm 1$ and $l_s = \pm 2$. The plot axes represent the camera pixels, with the corresponding scale shown for the $l_s = 1$ case, and the colorbars are expressed in coincidences per minute.

4. Conclusions

We have demonstrated an improved detection technique for OAM-entangled photon pairs, combining the use of a mode projector (based on a spatial light modulator and coupling into a single mode fiber) for the signal photon, and spatially-resolved detection with an ICCD camera for the idler photon. We project the signal photon onto an LG mode with a particular azimuthal index l_s and exploit the high resolution, high efficiency and short triggering times of a commercial ICCD camera so as to spatially-resolve the heralded idler photon in an LG mode with azimuthal index $l_i = -l_s$. We can thus directly visualize the OAM correlations $l_i = -l_s$ (for zero OAM in the pump $l_p = 0$) expected from conservation of OAM. By summing over the counts obtained in the pixels of the ICCD, we are able to obtain the OAM spectrum comprised of the expansion coefficients $\left|C_{(l,-l)}\right|^2$ of the quantum state in the LG basis. In addition, we ascertain the presence of OAM and measure the topological charge of the heralded idler photons through far-field diffraction by an equilateral triangular aperture. We believe that these results may prove useful in developing quantum communication protocols relying on the OAM and transverse spatial degrees of freedom.

Appendix A: optical and electronic delays

Taking advantage of the polarization of the idler photon, it is possible to reduce the complexity of the setup required for the image-preserving optical delay line (OD in Fig. 1), including the number of optical elements and the space needed on the optical table, by making the photon travel twice through three 1x telescopes, in a forward and backward folded-path configuration [29].

Optics EXPRESS

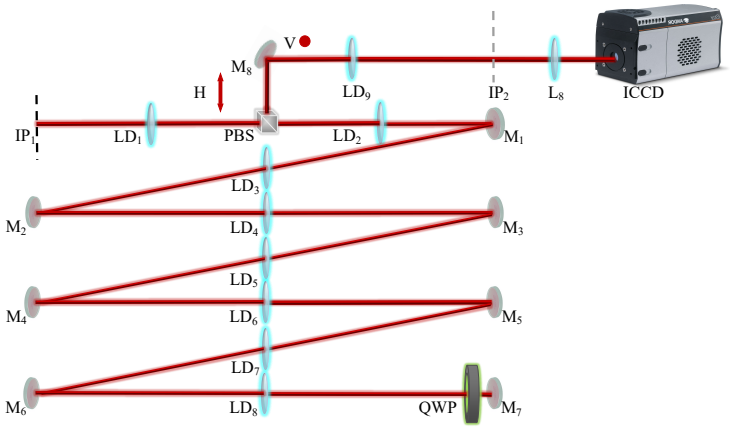

Fig. 8. Detail of the image-preserving optical delay line (OD).

In order to implement the OD shown in Fig. 8, the heralded idler photon at the crystal image plane IP_1 propagates with the *p*-polarization transmitted by the polarizing beam splitter PBS, placed at the focal plane of the first 1x telescope, formed by two bi-convex 2" diameter, 500*mm* focal length lenses (LD_1 and LD_2). In this manner, the idler photon traverses the PBS entering the next three consecutive 1x telescopes, formed by two bi-convex 2" diameter, 1000*mm* focal length lenses (LD_3 to LD_8). By placing a quarter wave plate (QWP) just before the last mirror (M_7), the idler photon experiences in total a $\lambda/2$ retardation, flipping the polarization from *p* to *s*. The polarization-rotated photon then propagates through the 1000*mm* 1x telescopes and then through the 500*mm* 1x telescope; this time it is reflected at the PBS, defining a new optical path which, with a third 2" diameter 500*mm* focal length lens (LD_9), which relays the propagated image to crystal image plane IP_2. Finally, in order to appreciate the spatial distribution of the idler photon it is necessary to observe the far-field of the image on plane IP_2. This is accomplished with the help of a plano convex 250*mm* focal length lens (L_8), yielding on plane FP_1 the Fourier transform of the image on plane IP_2.

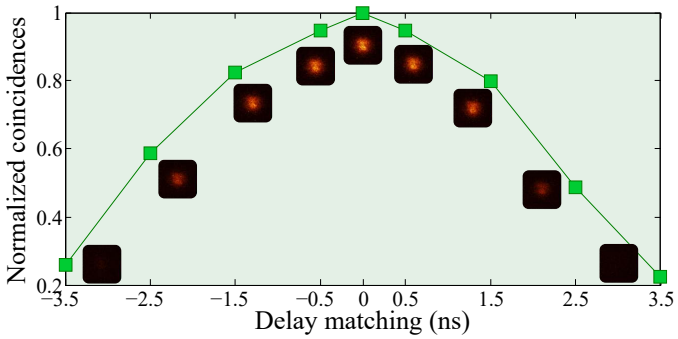

Fig. 9. Total normalized coincidence rate and the spatial mode distribution of the heralded idler photon for an acquisition time of 10s and for the specific case where the mode $l_s = 0$ is selected for the signal photon. The fine tuning in the electronic delay required for optimizing the image acquisition system can be appreciated. The zero delay configuration for which coincidence counts are maximized is used in the experiments presented.

Optics EXPRESS

In order to observe the spatial mode distribution of the heralded idler photon with the ICCD camera, we need to convert the positive-voltage TTL output electronic pulse generated for each detection event at the SPAD into the negative-voltage NIM electronic pulse which the gate generator in the camera accepts. To do so, each SPAD pulse is processed by a sequence of NIM modules which discriminates incoming pulses, controls their width, and introduces an electronic delay of up to $32ns$ (with $0.5ns$ resolution), in order to ensure the overlap of the detection gate at the ICCD and the arrival time of the idler photon. The temporal width of the generated NIM pulse defines the coincidence window of the detection system, which in our case is set to $10ns$. With this configuration, and by fine tuning the electronic delay in the NIM module, it is possible to make a direct measurement of the conditionally-prepared LG mode of the idler photon, as shown in Fig. 9.

Appendix B: complete set of measurements for the heralded idler photon

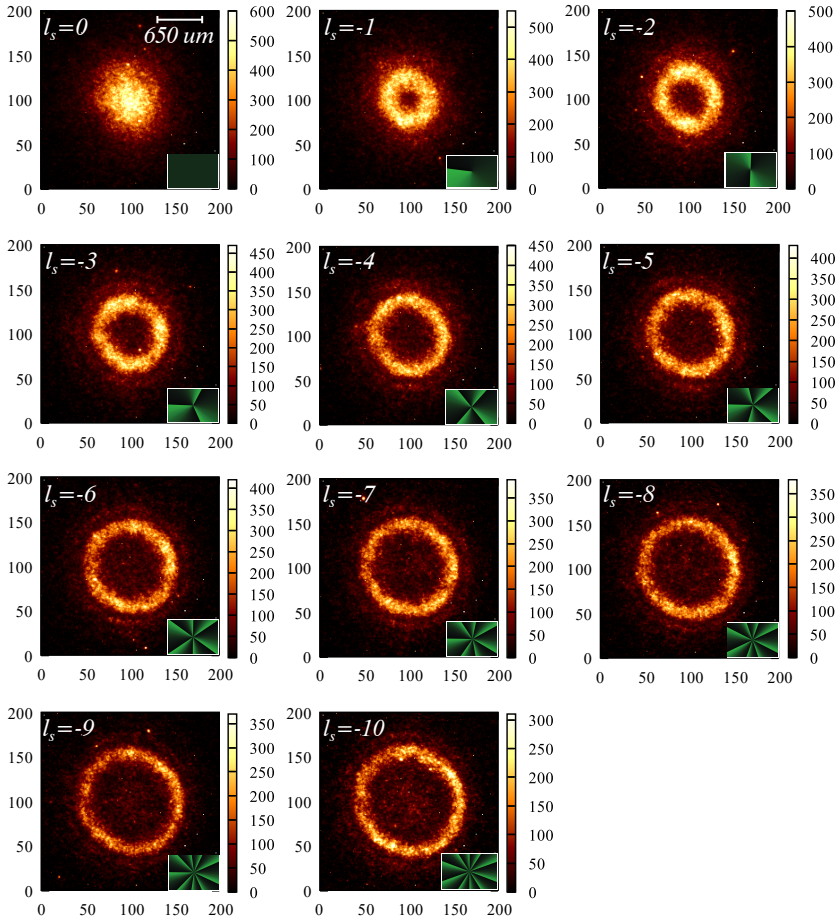

Fig. 10. Coincidence count rate recorded by the ICCD, representing the far-field transverse intensity distribution of the heralded idler photon for $l_s \leq 0$ values. The plot axes represent the camera pixels, with the corresponding scale shown for the $l_s = 0$ case, and the colorbars are expressed in coincidences per minute. The inset shows the phase mask displayed on the SLM.

Optics EXPRESS

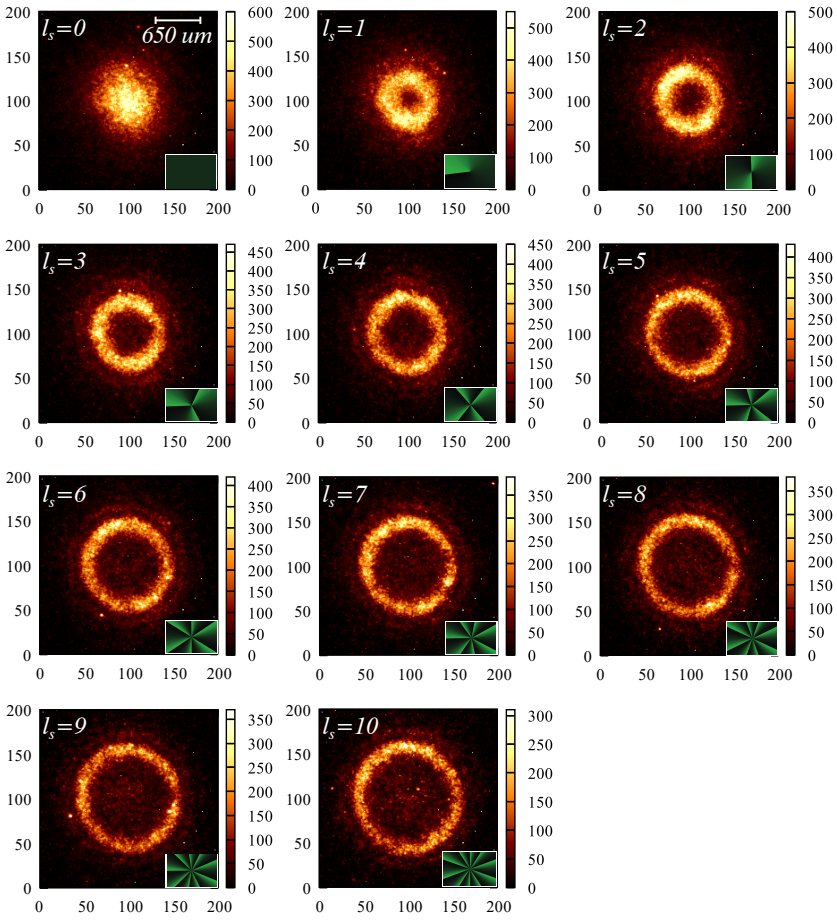

Fig. 11. Coincidence count rate recorded by the ICCD, representing the far-field transverse intensity distribution of the heralded idler photon for $l_s \geq 0$ values. The plot axes represent the camera pixels, with the corresponding scale shown for the $l_s = 0$ case, and the colorbars are expressed in coincidences per minute. The inset shows the phase mask displayed on the SLM.

Appendix C: method to align the equilateral triangular aperture

As the transverse positioning of the TA is critical, in order to align it we use the setup shown in Fig. 12, where a 1x magnification 4f telescope (L_9 with $f_9 = 100mm$ and L_{10} with $f_{10} = 100mm$) maps the TA plane to the ICCD camera plane IP_3. Then, the TA is carefully displaced with a $100nm$ resolution two-dimensional motor until centered on the mode singularity. When this is achieved, L_{10} is removed and the ICCD is moved forward to the Fourier plane of L_9 (FP_2) to observe the far-field diffraction patterns presented in Fig. 7.

Optics EXPRESS

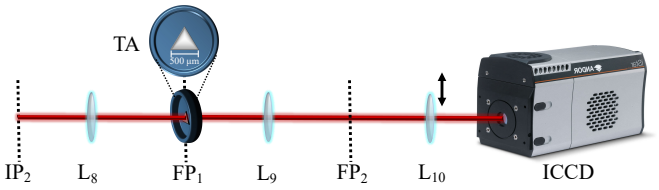

Fig. 12. Setup for aligning the equilateral triangular aperture (TA).

Funding

CONACYT, Mexico (293471, 293694, Fronteras de la Ciencia 1667); PAPIIT (UNAM) (IN104418); AFOSR (FA9550-16-1-1458).

Acknowledgments

We acknowledge support from CONAYCT, Mexico, PAPIIT (UNAM), and AFOSR.

References

1. N. B. Simpson, K. Dholakia, L. Allen, and M. J. Padgett, "Mechanical equivalence of spin and orbital angular momentum of light: an optical spanner," Opt. Lett. **22**, 52–54 (1997).
2. M. P. MacDonald, L. Paterson, K. Volke-Sepulveda, J. Arlt, W. Sibbett and K. Dholakia, "Creation and manipulation of three-dimensional optically trapped structures," Science **296**, 1101–1103 (2002).
3. T. Otsu, T. Ando, Y. Takiguchi, Y. Ohtake, H. Toyoda, and H. Itoh, "Direct evidence for three-dimensional off-axis trapping with single Laguerre-Gaussian beam," Sci. Rep. **4**, 4579–4586 (2014).
4. M. J. Padgett and R. Bowman, "Tweezers with a twist," Nat. Photon. **5**, 343–347 (2011).
5. G. Gibson, J. Courtial, M. J. Padgett, M. Vasnetsov, V. Pas'ko, S. M. Barnett, and S. Franke-Arnold, "Free-space information transfer using light beams carrying orbital angular momentum," Opt. Express **12**, 5448–5455 (2004).
6. L. Allen, M. W. Beijersbergen, R. J. C. Spreeuw, J. P. Woerdman, "Orbital angular momentum of light and the transformation of Laguerre-Gaussian laser modes," Phys. Rev. A **45**, 8185–8189 (1992).
7. H. Arnaut and G. Barbosa, "Orbital and intrinsic angular momentum of single photons and entangled pairs of photons generated by parametric down-conversion," Phys. Rev. Lett. **85**, 286–289 (2000).
8. Franke-Arnold, S. S. Barnett, M. J. Padgett, and L. Allen, "Two-photon entanglement of orbital angular momentum states," Phys. Rev. A **65**, 033823 (2002).
9. A. Mair, A. Vaziri, G. Weihs, and A. Zeilinger, "Entanglement of the orbital angular momentum states of photons," Nature **412**, 313–316 (2001).
10. A. C. Dada, J. Leach, G. S. Buller, M. J. Padgett, and E. Andersson, "Experimental high-dimensional two-photon entanglement and violations of generalized Bell inequalities," Nat. Phys. **7**, 677–680 (2011).
11. J. Leach, B. Jack, J. Romero, M. Ritsch-Marte, R.W. Boyd, A. K. Jha, S. M. Barnett, S. Franke-Arnold, and M. J. Padgett, "Violation of a Bell inequality in two-dimensional orbital angular momentum state-spaces," Opt. Express **17**, 8287–8293 (2009).
12. B. Jack, J. Leach, J. Romero, S. Franke-Arnold, M. Ritsch-Marte, S. M. Barnett, and M. J. Padgett, "Holographic ghost imaging and the Violation of a Bell Inequality," Phys. Rev. Lett. **103**, 083602 (2009).
13. T. Pittman, Y. Shih, D. Strekalov, and A. Sergienko, "Optical imaging by means of two-photon quantum entanglement," Phys. Rev. A **52**, R3429–R3432 (1995).
14. R. Fickler, M. Krenn, R. Lapkiewicz, S. Ramelow, and A. Zeilinger, "Real-time imaging of quantum entanglement," Sci. Rep. **3**, 1914 (2013).
15. E. Yao, S. Franke-Arnold, J. Courtial, M. J. Padgett, and S. M. Barnett, "Observation of quantum entanglement using spatial light modulators," Opt. Express **14**, 13089–13094 (2006).
16. A. H. Ibrahim, F. S. Roux, M. McLaren, T. Konrad, and A. Forbes, "Orbital-angular-momentum entanglement in turbulence," Phys. Rev. A **88**, 012312 (2013).
17. S. P. Walborn, A. N. de Oliveira, R. S. Thebaldi, and C. H. Monken, "Entanglement and conservation of orbital angular momentum in spontaneous parametric down-conversion," Phys. Rev. A **69**, 023811 (2004).
18. A. M Yao, "Angular momentum decomposition of entangled photons with an arbitrary pump," New J. Phys. **13**, 053048 (2011).
19. A. R. Altman, K. G. Köprülü, E. Corndorf, P. Kumar, and G. A. Barbosa, "Quantum imaging of nonlocal spatial correlations induced by orbital angular momentum," Phys. Rev. Lett. **94**, 123602 (2005).
20. M. McLaren, M. Agnew, J. Leach, F. S. Roux, M. J. Padgett, R. W. Boyd, and A. Forbes, "Entangled Bessel-Gaussian beams," Opt. Express **20**, 23589–23597 (2012).

Optics EXPRESS

21. Y. Jerónimo-Moreno and R. Jáuregui, "On-demand generation of propagation-invariant photons with orbital angular momentum," Phys. Rev. A **90**, 013833 (2014).
22. H. Cruz-Ramírez, R. Ramírez-Alarćon, F. J. Morelos, P. A. Quinto-Su, J. C. Gutiérrez-Vega, and A. B. U'Ren, "Observation of non-diffracting behavior at the single-photon level," Opt. Express **20**, 29761–29768 (2012).
23. V. Vicuña-Hernández, H. Cruz-Ramírez, R. Ramírez-Alarcón, and A.B. U'Ren, "Classical to quantum transfer of optical vortices," Opt. Express **22**, 20027–20037 (2014).
24. R. Ramírez-Alarcón, V. Vicuña-Hernández, H. Cruz-Ramírez, and A.B. U'Ren, "Transverse amplitude transfer experiments based on the process of spontaneous parametric downconversion," Phys. Scr. **90**, 068013 (2015).
25. R. Ramírez-Alarcón, H. Cruz-Ramírez and A. B. U'Ren, "Effects of crystal length on the angular spectrum of spontaneous parametric downconversion photon pairs," Laser Phys. **23**, 055204 (2013).
26. C. I. Osorio, G. Molina-Terriza, and J. P. Torres, "Correlations in orbital angular momentum of spatially entangled paired photons generated in parametric down-conversion," Phys. Rev. A **77**, 015810 (2008).
27. S. M. Barnett and R. Zambrini, "Orbital angular momentum of light," in *Quantum Imaging* (Springer, 2007), pp. 284.
28. S. J. van Enk and G. Nienhuis, "Eigenfunction description of laser beams and orbital angular momentum of light," Opt. Commun. **94**, 147–154 (1992).
29. R. S. Aspden, D. S. Tasca, R. W. Boyd and M. J. Padgett, "EPR-based ghost imaging using a single-photon-sensitive camera," New J. Phys. **15**, 073032 (2013).
30. W. Han, Y. Yang, W. Cheng, and Q. Zhan, "Vectorial optical field generator for the creation of arbitrarily complex fields," Opt. Express **21**, 20692–20706 (2013).
31. D. Klyshko, "A simple method of preparing pure states of the optical-field, a realization of the Einstein, Podolsky, Rosen experiment and a demonstration of the complementarity principle," Usp. Fiz. Nauk **154**, 133–152 (1988).
32. R. S. Aspden, D. S. Tasca, A. Forbes, R. W. Boyd, and M. J. Padgett, "Experimental demonstration of KlyshkoâĂŹs advanced-wave picture using a coincidence-count based, camera-enabled imaging system," J. Mod. Opt. **61**, 547–551 (2014).
33. J. M. Hickmann, E. J. S. Fonseca, W. C. Soares, and S. Chavez-Cerda, "Unveiling a truncated optical lattice associated with a triangular aperture using lights orbital angular momentum," Phys. Rev. Lett. **105**, 053904 (2010).
34. A. J. Jesus-Silva, E. S. Fonseca, and J. M. Hickmann, "Measurement of the orbital angular momentum at photon level via the spatial probability distribution," J. Mod. Opt. **59**, 1194–1198 (2012).